

Submitted to Ap. J. Letters; astro-ph/9612040

Whole Disk Observations of Jupiter, Saturn and Mars in Millimeter–Submillimeter Bands

A. B. Goldin¹, M. S. Kowitt¹, E. S. Cheng², D. A. Cottingham³, D. J. Fixsen⁴, C. A. Inman², S. S. Meyer¹, J. L. Puchalla², J. E. Ruhl⁵, and R. F. Silverberg²

ABSTRACT

Whole disk brightness ratios for Jupiter, Saturn, and Mars are reported at 5.7, 9.5, 16.4, and 22.5 cm⁻¹. Using models for the brightness temperature of Mars, the whole disk brightness temperatures for Jupiter and Saturn are also given for the four frequencies.

Subject headings: balloons — cosmic microwave background — infrared: solar system — planets and satellites: individual (Jupiter, Mars, Saturn) — radio continuum: solar system

1. Introduction

Whole-disk brightness temperature measurements of the planets are frequently used as calibrators for radio and infrared astronomy. For instruments with beam size larger than $\sim 1'$, planets are bright, unresolved sources ideal for mapping the shape of the far-field

¹Department of Astronomy and Astrophysics, and Enrico Fermi Institute, University of Chicago, 5640 South Ellis Avenue, Chicago, IL 60637

²Laboratory for Astronomy and Solar Physics, NASA/Goddard Space Flight Center, Code 685, Greenbelt, MD 20771

³Global Science and Technology, Inc., Laboratory for Astronomy and Solar Physics, NASA/GSFC Code 685, Greenbelt, MD 20771

⁴Hughes STX, Laboratory for Astronomy and Solar Physics, NASA/GSFC Code 685, Greenbelt, MD 20771

⁵Department of Physics, University of California, Santa Barbara, CA 93106

antenna pattern as well as providing an absolute calibration. In particular, for studies of anisotropy in the cosmic microwave background radiation (CMBR), precise common calibration targets are needed to permit comparison of experimental results with each other and with theories. Jupiter and Saturn, while bright and frequently observable, have complicated atmospheres which introduce substantial uncertainties in modeling their brightness temperatures. Mars, however, has only a tenuous CO₂ atmosphere which, for broad-band millimeter and submillimeter observations, can be safely neglected compared with thermal emission from the Martian surface (Griffin *et al.* 1986 and Wright 1976).

We report here the results of multi-frequency observations of Jupiter, Saturn, and Mars. Primary results are whole-disk brightness ratios of Mars to Jupiter, and Saturn to Jupiter; using model calculations of the Martian brightness temperature, we also present whole disk brightness temperatures for Jupiter and Saturn.

2. Instrument and Observation

The observations were performed with the Medium Scale Anisotropy Measurement, MSAM1, a balloon-borne instrument designed to measure anisotropy in the CMBR at 0.5 scales. This instrument has been described in Fixsen *et al.* 1996; only the salient features are reviewed here.

MSAM1 uses a 1.4 m off-axis Cassegrain telescope with a nutating secondary mirror for beamswitching. The main lobe of the telescope is 28' FWHM, and the beam follows a 2 Hz four phase square wave chop (i.e., center, left, center, right) with $\pm 40'$ amplitude. The telescope has a multimode feed, instrumented with a 4 band bolometric radiometer. The effective frequency and bandwidths of the four bands, using Rayleigh-Jeans color corrections, are given in Table 1. A gyroscope is aligned with the telescope main beam to provide an inertial reference, while absolute pointing is determined using a CCD star camera.

The observations were made in a flight from the National Scientific Balloon Facility in Palestine, Texas on 1995 June 2. At the beginning of the flight, we performed a raster scan across Jupiter to determine the antenna pattern, and then performed horizontal calibration scans across Jupiter and Mars for flux calibration. For the next 5 hours, the telescope executed deep scans above the North Celestial Pole to measure CMBR. After the CMBR observations, the telescope was again slewed to Jupiter. Another raster was performed to re-check the antenna pattern, followed by another calibration scan on Jupiter. Finally, a calibration scan was performed on Saturn. The detailed circumstances for each of the four

calibration scans are given in Table 2. Because the observations are made from balloon altitudes, atmospheric extinction is completely negligible. Of particular note is that, for these observations, the Saturn ring inclination angle to Earth is nearly zero ($-0^{\circ}.37$); thus, we are measuring only the disk.

3. Data Analysis

These planet observations have a high signal-to-noise ratio, even in the raw time-ordered data. This requires a somewhat different approach for the data reduction than that previously reported for CMBR anisotropy (Cheng *et al.* 1994, Cheng *et al.* 1996, and Inman *et al.* 1996). Systematic effects, particularly with regards to precise telescope pointing, are the limiting factors here.

3.1. Pointing

The accurate determination of the telescope orientation is critical for this measurement. We find the telescope pointing by matching star camera images against a star catalog. This fixes the position of the camera frame at the time of the exposure; between exposures, pointing is interpolated with the gyroscope outputs. Typically, the pointing drifts about $2'$ between successive camera exposures. The residual errors from interpolating between exposures is presumably several times smaller than this. The position of the main telescope beam within the camera frame is determined from the raster scan across Jupiter. Note that for the planetary observations, the image of the planet itself is deleted from the CCD frame, and background stars are used to establish the celestial coordinates of the beam. This ensures that blooming in the CCD due to the bright planet does not compromise the attitude solution. Noise in the gyroscope readout leads to a random RMS pointing uncertainty of $0'.7$.

3.2. Detector Data Reduction

In this analysis, we use a “double-difference” demodulation of the data. For each complete cycle of the secondary mirror, the data for the two side beams are averaged and subtracted from the average of the central beam data, producing a single demodulated value every 0.5 s for each of the four radiometer bands. This results in a symmetrical, three-lobe antenna pattern that is well suited to absolute flux determinations.

Table 1. Bandpass Integrals over Rayleigh-Jeans Spectrum ^a

Band	$\langle \nu \rangle$ (cm ⁻¹)	$\Delta\nu$ (cm ⁻¹)
1	5.73	1.32
2	9.54	2.39
3	16.4	1.82
4	22.5	1.32

^a The effective frequency and bandwidth are given by $\langle \nu \rangle = \frac{\int \nu F(\nu) I_\nu d\nu}{\int F(\nu) I_\nu d\nu}$, $\Delta\nu = \frac{\int F(\nu) I_\nu d\nu}{I_{\langle \nu \rangle}}$, where $I_\nu \propto \nu^2$ is a Rayleigh-Jeans spectrum and $F(\nu)$ is the filter function of the band (see, e.g., Page *et al.* 1994).

Table 2. Observation Circumstances for 1995 June 2

Scan	UT	Lat.	Long.	Alt. (km)	Elevation
Jupiter-1	03:41:51 – 03:49:12	31°19' N	95°41' W	34.9	25°32' – 26°30'
Mars	03:59:01 – 04:11:47	31°17' N	95°44' W	36.1	32°55' – 30°09'
Jupiter-2	09:47:05 – 09:53:49	31°28' N	98°27' W	37.6	18°56' – 17°48'
Saturn	10:11:03 – 10:17:13	31°23' N	98°39' W	37.3	30°07' – 31°15'

Slow offset drifts are present in the data, and must be removed. For each observation listed in Table 2, a single linear drift in time is fit to those portions of the data corresponding to times when the telescope was pointed well away from the target planet. This linear drift is then subtracted from the data. Since the observations are short and the drifts are slow, this simple model is adequate for dedrifting.

The detector signal contains transient spikes due to cosmic rays striking the detectors. In our previous analyses, the very low instantaneous signal-to-noise permitted the identification and removal of these transients directly from the time-ordered data. The presence of large signals from the target planets prevents this procedure; instead, a smooth spatial model is fit to the data, and cosmic ray spikes are identified as significant outliers from the fit. For the raster observations, each of the 9 horizontal scans was fit to a cubic spline with 30 uniformly-spaced knots. An initial noise estimate σ is formed from the RMS of the residuals from the fit, and then 3σ outliers are deleted. The fit is then repeated, and vertical splines are used to interpolate between the scan lines to form a $2^{\circ}8 \times 0^{\circ}9$ beammap. Finally, raw detector noise is estimated from the RMS of a subset of the data pointed at least $1^{\circ}4$ away from the target planet.

The calibration scans were analyzed in a similar way, except that instead of free splines, the fit model was constructed from the beammap derived in the raster analysis. For each datum in a calibration scan, the telescope pointing is used to determine a planetocentric X, Y coordinate, which is then referenced to obtain the beammap amplitude. A single free parameter, the overall scan-to-raster flux ratio, is then fit to the data. Again, 3σ outliers are deleted, and the fit is repeated. Between 2% and 8% of the data are removed this way, depending on scan. For this procedure, the early Jupiter raster is used for fitting the two scans at the beginning of the flight, while the late Jupiter raster is used for the two scans at the end of the flight. A systematic check on this processing is provided by the Jupiter calibration scans, which should yield a scan-to-raster flux ratio of 1 (within errors). The fit results are given in Table 3.

3.3. Error Analysis

Detailed Monte-Carlo simulations were used to estimate the errors on the scan-to-raster flux ratios. Each realization was generated by starting with the measured bolometer and pointing data, and adding normally distributed random numbers with variances corresponding to the estimated bolometer and position-readout noise, respectively. An additional random linear position drift, corresponding to the slow absolute pointing uncertainty, was also added to the simulated pointing data. Note that pointing noise

and drift were simulated in both azimuth and elevation. For each simulated dataset, we reconstruct the beammaps and scan-to-raster flux ratios according to the procedure described above. Final error estimates for the scan-to-raster flux ratios are determined from the standard deviation of the simulated ratios. In contrast to our CMBR measurements, here we find that the uncertainty is dominated by the position readout noise, and not the bolometer noise.

We note the presence among the Jupiter scan results in Table 3 of two values out of eight (Jupiter–1 band 1, and Jupiter–2 band 4) with greater than 2σ deviations from unity. This has $\sim 3\%$ probability (based on $\chi^2 = 17$ for 8 degrees of freedom), and so may be evidence of an additional unaccounted systematic error in the data. We have conservatively decided to inflate the estimated uncertainties that follow by a factor of 1.46, which forces the reduced χ^2 of the Jupiter scans to unity.

3.4. Whole-Disk Brightness Temperature Ratios

The raw flux ratios determined in §3.2 are converted to whole-disk brightness temperature ratios using the effective mm/sub-mm band planetary equatorial radii and ellipticities of Hildebrand *et al.* 1985: $R_{\text{eq}}(\varepsilon) = 3397$ (0.006), 71495 (0.065), and 60233 km (0.096) for Mars, Jupiter, and Saturn, respectively, along with their geocentric distances and polar inclinations at the epoch of observation.

These constitute the primary results reported here, and are given in Table 4. The errors reported in the table reflect the total uncertainty, as determined in §3.3, and include the extra scale factor (1.46).

Table 3. Ratios of Target Planet Flux to Jupiter Flux

Band	Jupiter–1	Mars	Jupiter–2	Saturn
1	1.036 ± 0.016	$(256 \pm 2.2) \times 10^{-4}$	0.979 ± 0.016	$(111 \pm 1.0) \times 10^{-3}$
2	1.016 ± 0.015	$(263 \pm 2.3) \times 10^{-4}$	0.994 ± 0.015	$(101 \pm 0.9) \times 10^{-3}$
3	1.011 ± 0.016	$(325 \pm 2.8) \times 10^{-4}$	0.993 ± 0.016	$(109 \pm 0.9) \times 10^{-3}$
4	0.985 ± 0.019	$(335 \pm 2.9) \times 10^{-4}$	1.044 ± 0.016	$(112 \pm 1.2) \times 10^{-3}$

4. Mars Models

To convert the brightness ratios into whole-disk brightness temperatures, an epoch-dependent thermal model of Mars is needed to provide an absolute calibration. We have used two distinct models for this purpose.

The first model considered (Wright 1976, Wright and Odenwald 1980) is extensively used in the literature (see, e.g., Hildebrand *et al.* 1985 and Griffin *et al.* 1986), and is based on 10–20 μm radiometer observations of Mars by the *Mariner 6 & 7* spacecraft. We follow the example of Hildebrand *et al.* 1985, and truncate this model assuming $T(\lambda \geq 350\mu\text{m}) = T(\lambda = 350\mu\text{m})$. The estimated model uncertainty at long wavelengths is $\pm 10\text{K}$ (Wright 1976).

The second model used (Rudy 1987, Rudy *et al.* 1987, Muhleman and Berge 1991) is based on a physical model of the dielectric properties of the upper meter of the Martian surface, constrained by polarized flux measurements obtained from *VLA* observations at $\lambda = 2$ and 6 cm. Some extrapolation is needed to estimate the properties of the regolith at our wavelengths; we have assumed a dielectric constant $\epsilon = 2.25 \pm 0.25$, and a power absorption length $l_\nu = (11 \pm 4)\lambda$ (Muhleman and Berge 1991). The model uncertainty due to the input parameter uncertainties (± 3 K) is somewhat smaller than that due to neglecting the effect of scattering (estimated at $\lambda = 2.7$ mm to be ± 6 K), giving a total model uncertainty of ± 7 K.

Both of these models involve substantial extrapolations in wavelength to reach our bands. We find it reassuring, however, that the two models, tuned to substantially different observations at very different wavelengths, give predicted brightness temperatures that agree well within their estimated uncertainties.

Table 4. Ratios of Target Planets Temperature to Jupiter Temperature

Band	Mars	Saturn
1	1.158 ± 0.015	0.833 ± 0.012
2	1.189 ± 0.015	0.758 ± 0.010
3	1.470 ± 0.019	0.818 ± 0.012
4	1.515 ± 0.019	0.840 ± 0.012

5. Brightness Temperatures

The modeled Mars temperatures, along with the derived whole-disk brightness temperatures for Jupiter and Saturn, are presented for both models in Table 5. Note that the errors listed reflect the uncertainty in the brightness ratios described in §3.3, but do not include the $\sim 5\%$ Mars model uncertainties which are common to all the points.

Figures 1 and 2 plot the brightness temperatures for Jupiter and Saturn using the Wright model for Mars; this is chosen to permit easy comparison with the earlier measurements of Ulich 1981, Hildebrand *et al.* 1985, and Griffin *et al.* 1986. Also plotted in the figures are two representative model temperature spectra, together with the series of molecular lines from which they are derived. The Jupiter models are from Griffin *et al.* 1986, and assume clear-sky (dashed) or NH_3 cloud cover with particle size $100 \mu\text{m}$ and a particle scale height to gas scale height ratio of 0.15 (dotted). The Saturn models are from Hildebrand *et al.* 1985, and assume an NH_3 mixing ratio of 2×10^{-4} in the deep atmosphere, and PH_3 mixing ratios equal to 1.5×10^{-6} (dashed) or 1.0×10^{-5} (dotted).

Note that our results at 16.4 cm^{-1} for both Jupiter and Saturn are significantly lower than previous measurements that cover this band. While we do not completely understand the cause of this, we offer several observations: The bandwidth of our 16.4 cm^{-1} filter is significantly narrower than the previous measurements (due to Hildebrand *et al.* 1985). This band is nearly coincident with the first expected strong dip in the spectra of the giant planets, near the $\sim 19 \text{ cm}^{-1}$ NH_3 and PH_3 resonances. Additionally, the measurements reported here had essentially 100% atmospheric transmission. The earlier measurements were made from the ground on Mauna Kea, and were corrected to a fixed value of the line of sight water vapor before taking ratios of unknown to calibration signals.

6. Conclusions

We have reported a new set of whole-disk brightness ratios for Mars, Jupiter, and Saturn which, when combined with a thermal model of Mars, give new calibration values for Jupiter and Saturn. The overall uncertainties on the brightness temperatures are still dominated by model uncertainty in the mm/sub-mm emission of Mars, but the ratio measurements presented here should remain useful well into the future, permitting a straightforward revision of the brightness temperatures of the giant planets with improvements in the Martian model. As was mentioned in Hildebrand *et al.* 1985, the effective mm/sub-mm emission radii of the gas giants are uncertain by as much as 1%, but while this uncertainty is important for understanding the precise brightness temperature

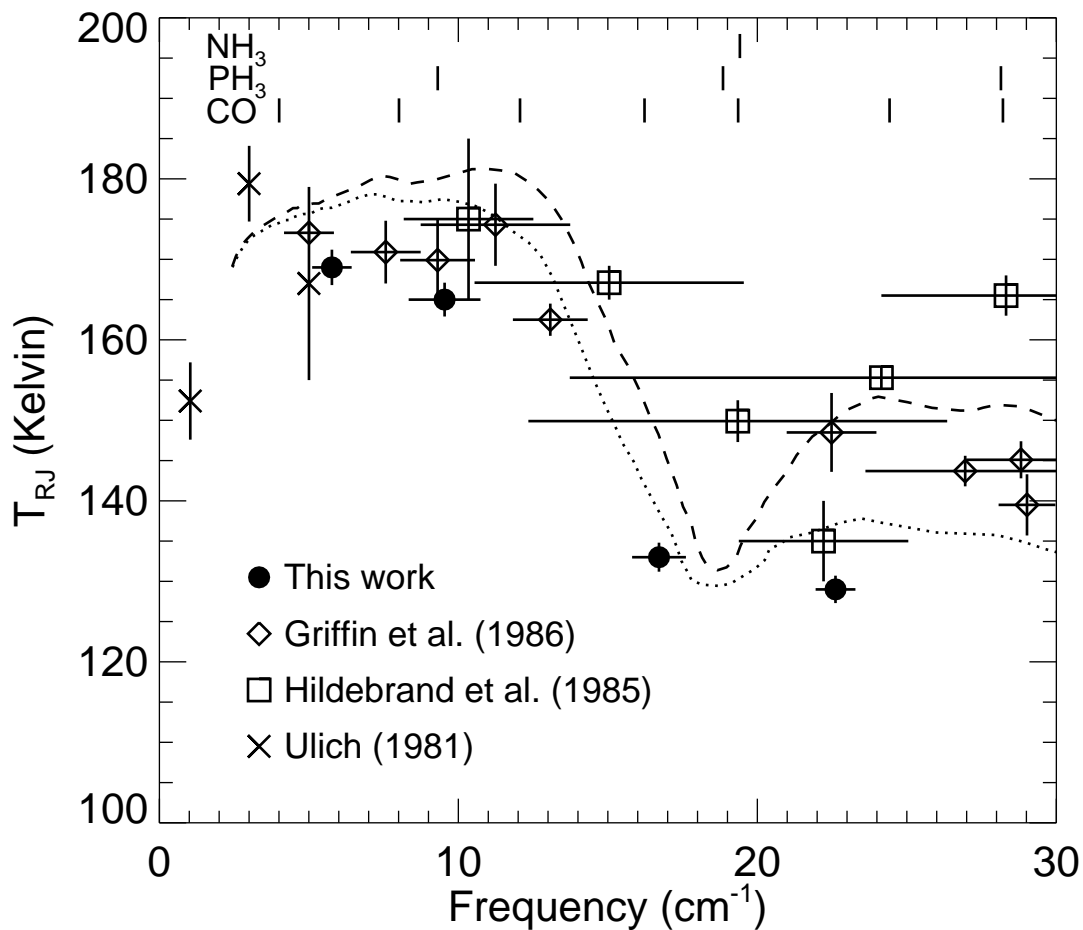


Fig. 1.— Whole-disk brightness temperatures for Jupiter. The Wright thermal model of Mars is used to determine the calibration. The vertical bars reflect the relative photometry errors, while the horizontal bars show the bandwidth of the measurements. The plotted errors do not include the Mars model uncertainty of $\pm 5\%$. The model spectra shown are from Griffin *et al.* 1986, and assume clear-sky (dashed) or NH_3 cloud with particle size $100 \mu\text{m}$ and a particle scale height to gas scale height ratio of 0.15 (dotted). The molecular lines from which they are calculated are shown at the top of the figure.

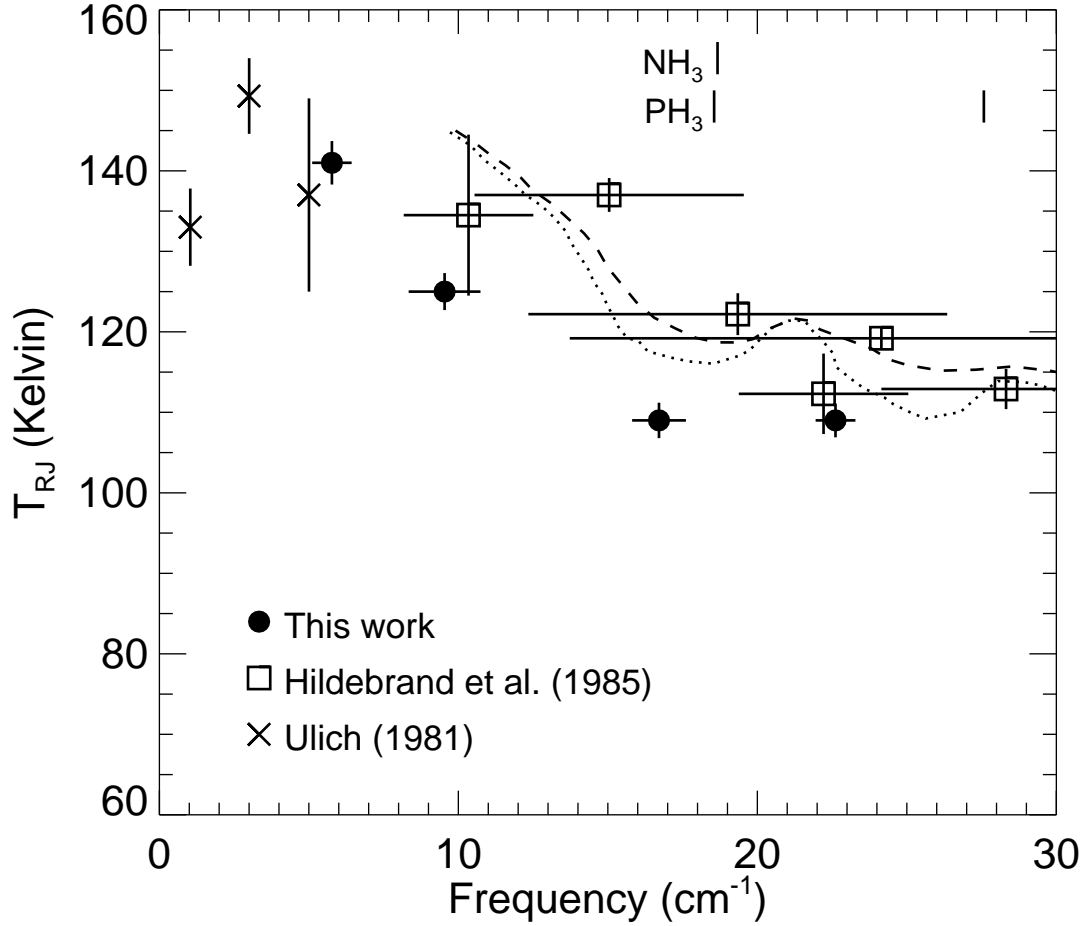


Fig. 2.— Whole-disk brightness temperatures for Saturn. The Wright thermal model of Mars is used to determine the calibration. The vertical bars reflect the relative photometry errors, while the horizontal bars show the bandwidth of the measurements. The plotted errors do not include the Mars model uncertainty of $\pm 5\%$. The model spectra shown are from Hildebrand *et al.* 1985, and assume an NH_3 mixing ratio of 2×10^{-4} in the deep atmosphere, and PH_3 mixing ratios equal to 1.5×10^{-6} (dashed) or 1.0×10^{-5} (dotted). The molecular lines from which they are calculated are shown at the top of the figure.

of the planet, it does not affect the total flux density, and thus is not an issue for use in large-beam calibration studies.

We would like to thank E. Weisstein and D. Muhleman for several useful discussions on the thermal model for Mars. We also thank the Free Software Foundation for the GNU software tools, and J. W. Eaton for Octave, both of which were extensively used in this work. This research was supported by the National Aeronautics and Space Administration through the Office of Space Science.

Table 5. Temperatures of planets.

Band	Wright model ($T = T_{350\mu m}$)			Rudy model (extrapolated)		
	Mars	Jupiter	Saturn	Mars	Jupiter	Saturn
1	196	169 ± 2	141 ± 3	196	169 ± 2	141 ± 3
2	196	165 ± 2	125 ± 2	198	166 ± 2	126 ± 2
3	196	133 ± 2	109 ± 2	201	137 ± 2	112 ± 2
4	196	129 ± 2	109 ± 2	203	134 ± 2	112 ± 2

The tabulated errors do not include the Mars model uncertainty of $\pm 10\text{K}$ (Wright) or $\pm 7\text{K}$ (Rudy).

REFERENCES

- Cheng, E. S. *et al.* 1994, ApJ, **422**, L37.
- Cheng, E. S. *et al.* 1996, ApJ, **456**, L71.
- Fixsen, D. J. *et al.* 1996, ApJ, **470**, 63.
- Griffin, M. J., Ade, P. A. R., Orton, G. S., Robson, E. I., Gear, W. K., Nolt, I. G., and Radostitz, J. V. 1986, Icarus, **65**, 244.
- Hildebrand, R. H. *et al.* 1985, Icarus, **64**, 64–87.
- Inman, C. A. *et al.* 1996, ApJ. submitted, preprint astro-ph/9603017.
- Muhleman, D. O. and Berge, G. L. 1991, Icarus, **92**, 263.
- Page, L. A., Cheng, E. S., Golubovic, B., Gundersen, J., and Meyer, S. S. 1994, Appl. Opt., **33**, 11.
- Rudy, D. J. 1987. *Mars: High Resolution VLA Observations at Wavelength of 2 and 6 cm and Derived Properties*. PhD thesis, California Institute of Technology.
- Rudy, D. J., Muhleman, D. O., Berge, G. L., Jakosky, B. M., and Christensen, P. R. 1987, Icarus, **71**, 159.
- Ulich, B. L. 1981, AJ, **86**, 1619.
- Wright, E. L. 1976, ApJ, **210**, 250.
- Wright, E. L. and Odenwald, S. 1980, BAAS, **12**, 456.